

Article

New Ionic Liquid Microemulsion-Mediated Synthesis of Silver Nanoparticles for Skin Bacterial Infection Treatments

Fayez Althobaiti ¹, Ola A. Abu Ali ², Islam Kamal ³ , Mohammad Y. Alfaifi ⁴ , Ali A. Shati ⁴, Eman Fayad ¹ , Serag Eldin I. Elbehairi ^{3,5} , Reda F. M. Elshaarawy ^{6,7,*}  and W. Abd El-Fattah ^{8,9,*} 

- ¹ Department of Biotechnology, Faculty of Sciences, Taif University, P.O. Box 11099, Taif 21944, Saudi Arabia
² Department of Chemistry, College of Science, Taif University, P.O. Box 11099, Taif 21944, Saudi Arabia
³ Department of Pharmaceutics, Faculty of Pharmacy, Port Said University, Port Said 42526, Egypt
⁴ Biology Department, Faculty of Science, King Khalid University, Abha 62529, Saudi Arabia
⁵ Cell Culture Lab, Egyptian Organization for Biological Products and Vaccines (VACSERA Holding Company), 51 Wezaret El-Zeraa St., Agouza, Giza 12654, Egypt
⁶ Department of Chemistry, Faculty of Science, Suez University, Suez 43533, Egypt
⁷ Institut für Anorganische Chemie und Strukturchemie, Heinrich-Heine Universität Düsseldorf, 40204 Düsseldorf, Germany
⁸ Chemistry Department, College of Science, IMSIU (Imam Mohammad Ibn Saud Islamic University), P.O. Box 5701, Riyadh 11432, Saudi Arabia
⁹ Department of Chemistry, Faculty of Science, Port Said University, Port Said 42526, Egypt
* Correspondence: reda.elshaarawy@suezuniv.edu.eg (R.F.M.E.); wabdulfatah@imamu.edu.sa (W.A.E.-F); Tel.: +20-101-7377216 (R.F.M.E.)

Abstract: This work reports a new approach for the synthesis of extremely small monodispersed silver nanoparticles (AgNPs) (2.9–1.5) by reduction of silver nitrate in a new series of benzyl alkyl imidazolium ionic liquids (BAILs)-based microemulsions (3a–f) as media and stabilizing agents. Interestingly, AgNPs isolated from the ILMs bearing the bulkiest substituents (*tert*-butyl and *n*-butyl) (3f) displayed almost no nanoparticle agglomeration. In an *in vitro* antibacterial test against ESKAPE pathogens, all AgNPs-BAILs had potent antibiotic activity, as reflected by antibacterial efficiency indices. Furthermore, when compared to other nanoparticles, these were the most effective in preventing biofilm formation by the tested bacterial strains. Moreover, the MTT assay was used to determine the cytotoxicity of novel AgNPs-BAILs on healthy human skin fibroblast (HSF) cell lines. The MTT assay revealed that novel AgNPs-BAILs showed no significant toxic effects on the healthy cells. Thus, the novel AgNPs-BAILs microemulsions could be used as safe antibiotics for skin bacterial infection treatments. AgNPs isolated from BAIL (3c) was found to be the most effective antibiotic of the nanoparticles examined.

Keywords: benzyl alkyl imidazolium ionic liquids; microemulsions; silver nanoparticles; antibacterial; skin bacterial infection treatments



Citation: Althobaiti, F.; Abu Ali, O.A.; Kamal, I.; Alfaifi, M.Y.; Shati, A.A.; Fayad, E.; Elbehairi, S.E.I.; Elshaarawy, R.F.M.; El-Fattah, W.A. New Ionic Liquid Microemulsion-Mediated Synthesis of Silver Nanoparticles for Skin Bacterial Infection Treatments.

Antibiotics **2023**, *12*, 247. <https://doi.org/10.3390/antibiotics12020247>

Academic Editor: Charlotte A. Huber

Received: 20 December 2022

Revised: 19 January 2023

Accepted: 20 January 2023

Published: 25 January 2023



Copyright: © 2023 by the authors. Licensee MDPI, Basel, Switzerland. This article is an open access article distributed under the terms and conditions of the Creative Commons Attribution (CC BY) license (<https://creativecommons.org/licenses/by/4.0/>).

1. Introduction

The exponential increase in bacterial-induced pathogenic infection has created a serious threat to global human health. The ESKAPE pathogens (*Staphylococcus aureus* (SA), *Klebsiella pneumoniae* (KP), *Pseudomonas aeruginosa* (PA), *Enterococcus faecium* (EF), *Acinetobacter baumannii* (AB), and *Enterobacter* species) have been assigned as the most deadly bacteria by the Infectious Diseases Society of America (IDSA). Antimicrobial agents (AMAs) effectively protect humans from these potentially fatal pathogenic micro-organisms [1,2]. However, many bacterial strains acquired tolerance to antibiotics long before humans began mass-producing them to prevent and cure infectious illnesses [3]. Further, the emergence of antimicrobial-resistant microbes has sparked a worldwide crisis due to antibiotic overuse and the limited effectiveness of conventional antibiotic therapy. Consequently, research for novel antimicrobial agents is urgently required to address this issue.

Recently, nanomaterials (NMs) have attracted a lot of attention from scientists and found widespread usage in many biological applications [4–7]. Among the different nanomaterials, noble metal nanoparticles (NMNPs) have gained great attention in the development of a diversity of smart multifunctional NMs for biomedical applications, owing to their non-toxicity and excellent intrinsic properties [8]. Aside from being surface active, NMNPs can release bioactive metal ions into biological systems, resulting in the induction of multiple modes of bioactivity.

There has been extensive research into nanosystems for drug delivery because of its attractive biodegradability, biocompatibility, specificity/selectivity, and low toxicity. In addition to its useful properties including biocompatibility and durability, non-immunogenicity, a large surface area, a high drug loading capacity, and a minimal leakage of medications, they can also be employed to the targeted administration of pharmaceuticals [9]. Over the past two decades, the use of metal nanoparticles (MNPs) as nanocarriers has drastically evolved due to their numerous advantages and benefits. Their unique physical, chemical, and biological properties are in the forefront of these advantages. Additionally, their small size allows them to traverse through biological barriers and release drugs at a desired target site [10]. Moreover, MNPs possess high loading capacity, surface-area-to-volume ratio, and can be easily functionalized with a variety of ligands to modulate the drug release profile. Therefore, MNPs have been successfully used in a range of drug delivery systems, including transdermal, oral, and injectable delivery [11]. Despite the advantages, the use of MNPs as nanocarriers is still in its infancy due to several current challenges. For example, the toxicity of MNPs, the difficulty in controlling their size and shape, and poor biocompatibility are several factors that need to be addressed [10].

Despite several studies reporting on the biological and therapeutic applications of NMNPs, particularly AgNPs [12–14], there have been very few reports on the use of ionic liquid-supported AgNPs (PdNPs-ILs) in these disciplines. For instance, Dorjnamjin et al. reported the synthesis of uniform monodisperse crystalline Ag nanoparticles mediated by two different series of hydroxyl functionalized ionic liquids (HFILs) and hydroxyl functionalized cationic surfactants (HFCs). AgNPs isolated from various ionic liquids exhibited promising in vitro antimicrobial activities against a range of Gram-positive and Gram-negative bacteria and fungi [15]. In addition, a room temperature ionic liquid (2-amino-1-dodecylpyridinium bromide) was used to prepare AgNPs (2–20 nm) with excellent antibacterial activity against *S. aureus*, *E. coli*, and *P. aeruginosa* [16]. AgNPs anchored in poly(ionic liquid) mesoporous nanocomposite (Ag-PIL) were recently synthesized by in situ reduction of AgNO₃ in PIL and used for controlled anticancer drug delivery with an antimicrobial effect. The Ag-PIL nanocomposite demonstrated outstanding bacteriostatic and bactericidal activity against both *E. coli* and *S. aureus* [17].

Notably, one of the drawbacks of using MNPs is their proclivity to agglomerate and aggregate as a result of the Ostwald ripening process [18]. This significantly reduces their stability and limits their utility in pharmaceutical applications [19]. Therefore, the MNPs should be stabilized either sterically or electrostatically to prevent agglomeration [19]. Benzyl alkyl ionic liquids (BAILs) could offer a promising solution for steric and electrostatic stabilizing of MNPs [20]. Electrostatic and steric interactions between MNPs and ILs contribute to their stabilization without affecting surface characteristics [21,22]. Furthermore, the ILs' strong ionic strength, polarity, and dielectric constant make them suitable mediums for the preparation and stabilization of MNPs [22]. On the other hand, among the various reported methods for synthesizing NMNPs [23], the microemulsion approach has attracted the attention of many researchers worldwide due to its simplicity, cost-effectiveness, and efficiency to produce stable NPs [24,25].

Motivated by these astounding facts and as a new step in our ongoing journey to explore and develop novel pharmacological agents [26–28], the present study reports the synthesis of new BAILs for application in the preparation and stabilization of AgNPs. In this study, several BAIL aggregation effects will be investigated as a function of the phenyl and imidazolyl substituents. Furthermore, the effects of various produced AgNPs

on ESKAPE pathogens as well as healthy human skin fibroblast (HSF) cell lines will be examined.

2. Results and Discussion

2.1. Synthesis

Using substituted alkylbenzenes and alkyl imidazoles as building blocks, a three-step methodology is developed to produce the desired benzyl alkyl ionic liquids (BAILs) (See Figure 1). First, alkylbenzenes (cumene and tert-butylbenzene) were chloromethylated with a chloromethylating agent mixture of dimethoxymethane-chlorosulfonic acid-ZnI to produce the appropriate chlorobenzyl derivatives (**1a–c**). Following that, N-benzyl imidazolium chlorides (**2a–f**) were synthesised by quaternizing 1-alkylimidazoles with chlorobenzyl derivatives under refluxing conditions in an inert atmosphere. Eventually, the counterparts imidazolium bis-((trifluoromethyl)sulfonyl) imide ionic liquids (**3a–f**) were obtained by subjecting these ILs to anion (chloride) metathesis with LiTf₂N at room temperature. On the other hand, the AgNPs were successfully produced using hydrazine hydrate-catalyzed AgNO₃ reduction in BAILs/TX-100/H₂O microemulsions. The colour change of water-BAIIL microemulsion containing Ag⁺ ions from a light yellow to a brownish yellow is indicative of the AgNPs formation. In this reduction process, BAAIL acts as a green solvent and stabilizing agent (Figure 1).

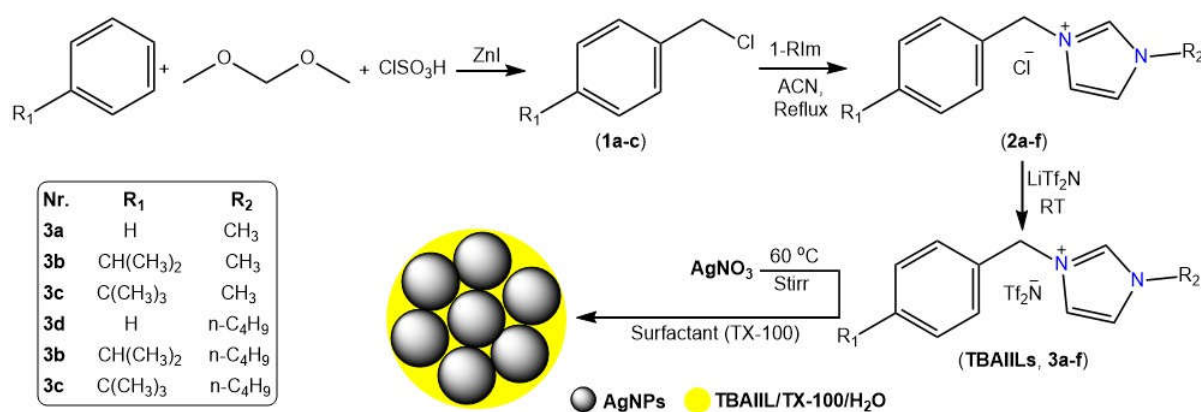


Figure 1. Stepwise synthesis of BAILs (**3a–f**) their applications in the synthesis of AgNPs.

2.2. Physical Characterization

BAILs were produced in excellent yields (85–95%) overall and they were physically characterized based on their appearance, solubility, lipophilicity, viscosity, and thermal stability measurements.

2.2.1. Physical Appearance, Solubility, and Lipophilicity

It is well established that the aqueous solubility and lipophilic properties of a new pharmacological agent are directly related to its pharmacokinetics and pharmacodynamics. It was for this reason that the room-temperature aqueous solubility of the novel BAILs was studied. All BAILs were found to be soluble in water, though each BAAIL dissolved in different degree depending on its structure. The degree to which they are soluble in water is controlled by the type of alkyl substituent present on the benzene and imidazole rings (see Table 1). For example, the tert-butylbenzylimidazolium cation (**3f**), which bears the most hydrophobic side chain (n-butyl), is the least soluble of the group (LogS = −8.163), while the benzylmethylimidazolium cation (**3a**) has the highest solubility (LogS = −5.719).

Table 1. Physicochemical characteristics of new BAILs.

TAAI.	MW (g/mol)	Appearance	LogS ^a	CLogP ^b	D (g/cm ³) ^c	η (cP) ^d	T _{dec} (°C) ^e
3a	453.37	Yellow oil	−5.719	−0.352	1.468	421.15	407
3b	495.46	Orange oil	−6.820	−0.262	1.397	426.85	402
3c	509.48	Yellow oil	−7.150	0.137	1.551	439.25	412
3d	495.46	Orange oil	−6.735	−0.102	1.298	512.67	397
3e	537.54	Brown oil	−7.834	1.325	1.213	521.83	394
3f	551.56	Orange oil	−8.163	1.724	1.311	543.25	401

^{a,b} calculated using ChemDraw 16; ^c density measured using COSMOtherm at 50 °C; ^d viscosity measured at 25 °C using a capillary viscometer; ^e decomposition temperature from DTG curves.

CLogP measurements demonstrate that the benzyl-alkylimidazolium cation is the least lipophilic cation, with a range from (−0.352) to (−0.102) depending on the nature of the alkyl substituent used (see Table 1). In contrast, replacing the hydrogen atom on the benzene ring with more hydrophobic groups such as *iso*-propyl and *tert*-butyl has significantly increased the CLogP values to be in the range of (−0.262)–(1.325) and (0.137)–(1.724), respectively, confirming their great lipophilic character. Interestingly, ionic liquids interact strongly with the outer lipophilic layer of microbial cell surfaces when they have a high CLogP value, and consequently their lipophilicity is increased [29].

2.2.2. Viscosity and Thermal Stability

Notably, IL-viscosity exhibits a great influence on the formation, molecular diffusion, and stability of nanoparticles. The stability of nanoparticles is greatly enhanced by the fact that their diffusion is greatly reduced in extremely viscous media like ionic liquids, which results in a lifetime increase of a factor of 10–1000 compared to that in traditional low viscosity solvents [30]. Ionic liquids also have the added benefit of reducing the likelihood of agglomeration of colloidal nanoparticles by suppressing their thermal motion due to the high viscosity. Therefore, the viscosities of new BAILs were measured at 25 °C, and the results are shown in Table 1. High viscosity values (421.15–543.25 cP) were observed for all imidazolium ILs; however, these values varied according to the cation's intrinsic structural characteristics. For example, out of all of the examined ionic liquids, the one with the lowest viscosity (428.75 cP) was BAIL 3a, which was made up of the simplest cation (benzyl-methylimidazolium). In contrast, *tert*-butylbenzyl group-containing BAIL 3f showed the greatest viscosity (543.25 cP). The very hydrophobic Tf₂N anion exerts stronger ion–ion interactions with the hydrophobic *tert*-butylbenzyl-methylimidazolium cation, which leads to the observed behavior of an increase in viscosity [29].

On the other hand, the thermal stabilities of BAILs (3a–f) were verified using their thermogravimetric (TG) curves (Figure S1, Supplementary Materials). All BAILs are clearly thermally stable up to about 400 °C before undergoing a sudden decline in their masses between 400 and 450 °C. Table 1 and Figure S1 (Supplementary Materials) show that BAILs with long side chains (*n*-butyl) linked to the imidazolium ring (3e–f) had more complex thermal degradation patterns and lower decomposition temperatures than BAILs containing methylimidazolium cation (3a–c).

2.3. Structural Characterization

Spectral investigations (FTIR, NMR (¹H, ¹³C, ¹⁹F), and ESI-MS) were used to deduce the structural formulae of all the synthesized BAILs.

2.3.1. Mass Spectrometry

To acquire a first perception of the characteristics of their cation and anion' structures, the electrospray ionization mass spectra (ESI-MS) of BAILs can be a helpful tool. In light of this, the ESI-MS of BAIL (3f) (Figure 2A) was extensively studied as a representative of new BAILs. The major peak was found at an *m/z* value of 271.3, which corresponds to the molar mass of a single-charged cation, [M – Tf₂N[−]]⁺, generated by the elimination of the bonded

anion. In addition, the fragmentation peaks that can be seen at m/z 214.4, 157.5, and 57.3 (base peak) could be assigned to consecutive removal of butyl side chains and benzyl-butylimidazolium radicals from the parent molecule, respectively, $[M - Tf_2N^- - C_4H_9]^+$, $[M - Tf_2N^- - 2(C_4H_9)]^+$, and $[M - Tf_2N^- - BnBIm]^+$.

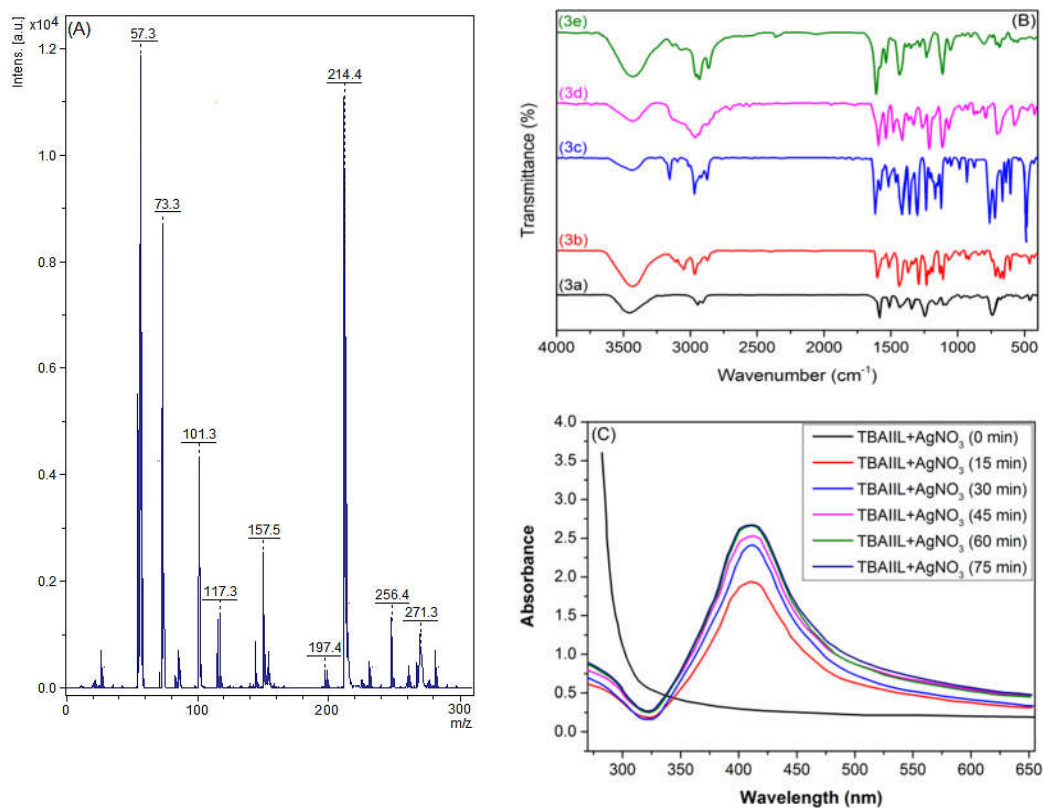


Figure 2. (A) A positive mode electrospray ionization mass spectra (ESI-MS (+ve)) of BAAIL (3f); (B) FTIR spectra of the native BAAILs (3a–f); and (C) UV-Vis spectrum AgNPs produced by BAAIL (3f).

2.3.2. FTIR Spectroscopy

The FTIR spectra of the new BAAILs (Figure 2B) were studied in an effort to learn more about the structural features of the cations and anions that make them up. The spectra of the TAILs exhibit absorption bands that are analogous to those of previously reported imidazolium-based ILs [31–33]. The common absorption peaks that can be seen in the FTIR spectra of BAAILs at 3110, 2970, 1591, 1245, 875, and 707 cm^{-1} could be attributed to the vibrational modes of the benzylimidazolium cation fragments, including imidazolium C2-H, alkyl C-H, imidazolium C=N, and the benzyl moiety, respectively [31]. In addition, the distinctive vibration bands of (TN_2f) anion may be observed in the regions of 1271 ± 3 cm^{-1} ascribed to $\nu_{as}(CF_3 + SO_2)$; 1224 ± 2 cm^{-1} due to $\nu_s(CF_3 + SO_2)$; 1139 ± 4 cm^{-1} typical for $\nu_{as}(CF_3 + CS)$; 1024 ± 3 and 911 ± 3 cm^{-1} for $\nu(N-S)$; 710 ± 5 cm^{-1} for $\delta(CF_3)$; and 747 ± 3 cm^{-1} assigned to $\nu(C-S)$ [34].

2.3.3. UV-Vis Spectroscopy

Figure 2C shows UV-Visible spectra of the BAAIL (3f)-based microemulsion containing $AgNO_3$ at time intervals as well as the progress in the formation of BAAIL-stabilized AgNPs with time. The appearance of a new peak at 430 nm in the microemulsion spectrum, which is characteristic of the surface plasmon resonance (SPR) of AgNPs [35], verifies the synthesis of AgNPs. Further, the SPR peak intensity rises with time, reflecting an increase in AgNPs yield, until it reaches a maximum value at 60 min. Thereafter, the peak intensity almost stops rising, denoting the end of the reaction.

2.3.4. NMR Spectroscopy

NMR spectra of new BAIILs were utilized to verify their successful production and provide a striking visual representation of the structure of their ions. However, due to the fact that all new BAIILs have nearly identical NMR spectra, with the exception of the peak of alkyl side chains, the $^1\text{H}/^{13}\text{C}$ NMR spectra of BAIIL (3e) (Figure 3) were analyzed in more detail as a representative of new BAIILs. As shown in the ^1H NMR spectrum of 3e, the proton resonance of imidazolium (C2-H) can be seen as a singlet at 9.91 ppm. Furthermore, a group of signals was detected in the chemical shift region of 7.93–7.12 ppm, assignable to the resonances of the imidazolium and phenyl protons. In addition, the benzylic protons can be seen as a singlet peak at 5.64. As for the protons of alkyl side chains (isopropyl and n-butyl groups), the methine and methyl protons of the isopropyl group emerged as septet (3.28 ppm) and doublet (1.21 ppm), respectively. While the methylene and methyl protons of the n-butyl group can be observed as a set of multiplets in the high-field region (4.26–0.91 ppm). The ^{13}C NMR spectrum of 3e, on the other hand, shows the carbon map in detail for both the central benzyliimidazolium cation and the alkyl substituents. The carbon signals characteristic of the benzyliimidazolium cation can be detected in the low-field region (146.03–122.54 ppm) for the resonances of the imidazolium and phenyl carbon atoms, while it is 55.75 for benzylic carbon. In contrast, the peaks distinctive of C-atom of alkyl substituents can be seen in the high-field region, 32.38 and 23.23 ppm for methine and methyl carbons of the isopropyl group; and 47.45, 31.82, 19.84, and 13.76 ppm for carbon atoms of n-butyl group. It is worth noting that the low-field carbon signal observed at 149.65 could be assigned to CF_3 of Tf_2N anion [29].

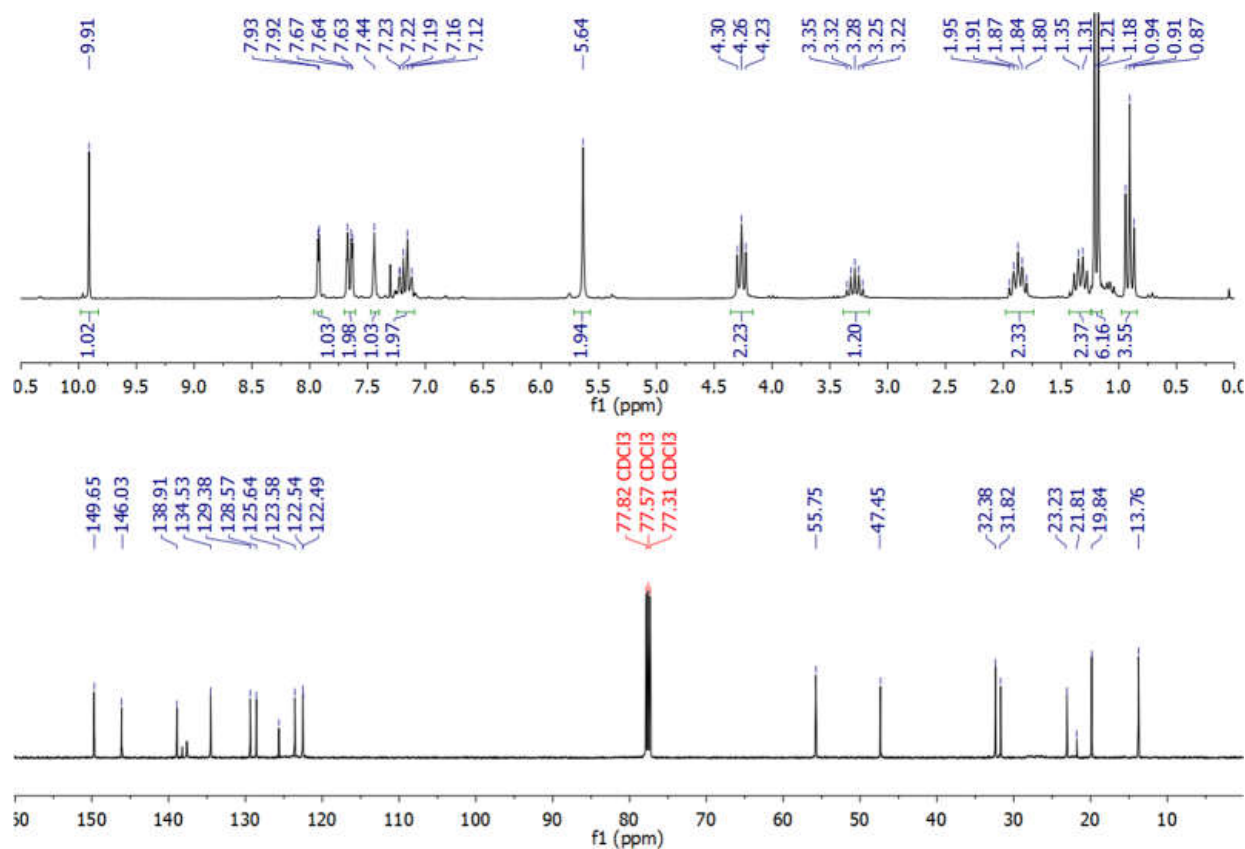


Figure 3. ^1H NMR (200 MHz) and ^{13}C NMR (125 MHz) of BAIIL (3e) in CDCl_3 .

2.4. Morphological Characterization

2.4.1. Transmission Electron Microscopy (TEM) Analysis

Representative TEM images of AgNPs obtained from hydrazine reduction of AgNO₃ in various BAIIIs are shown in Figure 4. When AgNO₃ is reduced in the presence of new BAIIIs, discrete AgNPs with diameters in the range of 2.9–1.5 nm are formed (from TEM). More agglomeration can be seen in the AgNPs made from the methylimidazolium-supported BAIIIs (3a–c) (Figure 4A–C) than in those made from the butylimidazolium-supported BAIIIs (3d–f) (Figure 4D–F). Meanwhile, the primary AgNPs produced by 4-iso-propylbenzyl- or 4-tert-butylbenzyl-substituted BAIIIs (3b, 3c, 3e, and 3f) were more separated than those produced by unsubstituted benzyl-based BAIIIs (3a,d). This could be due to the electrostatic and steric interactions between AgNPs and BAIIIs, which contribute to their stabilization without affecting surface characteristics by forming a protecting layer that prevents AgNPs coalescence [21,22]. Unlike more traditional approaches, this synthetic process permits the synthesis of AgNPs networks with narrower particle size dispersion. Interestingly, AgNPs isolated from the BAIII bearing the bulkiest substituents (*tert*-butyl and *n*-butyl) (3f) displayed almost no NPs agglomeration (see Figure 4E).

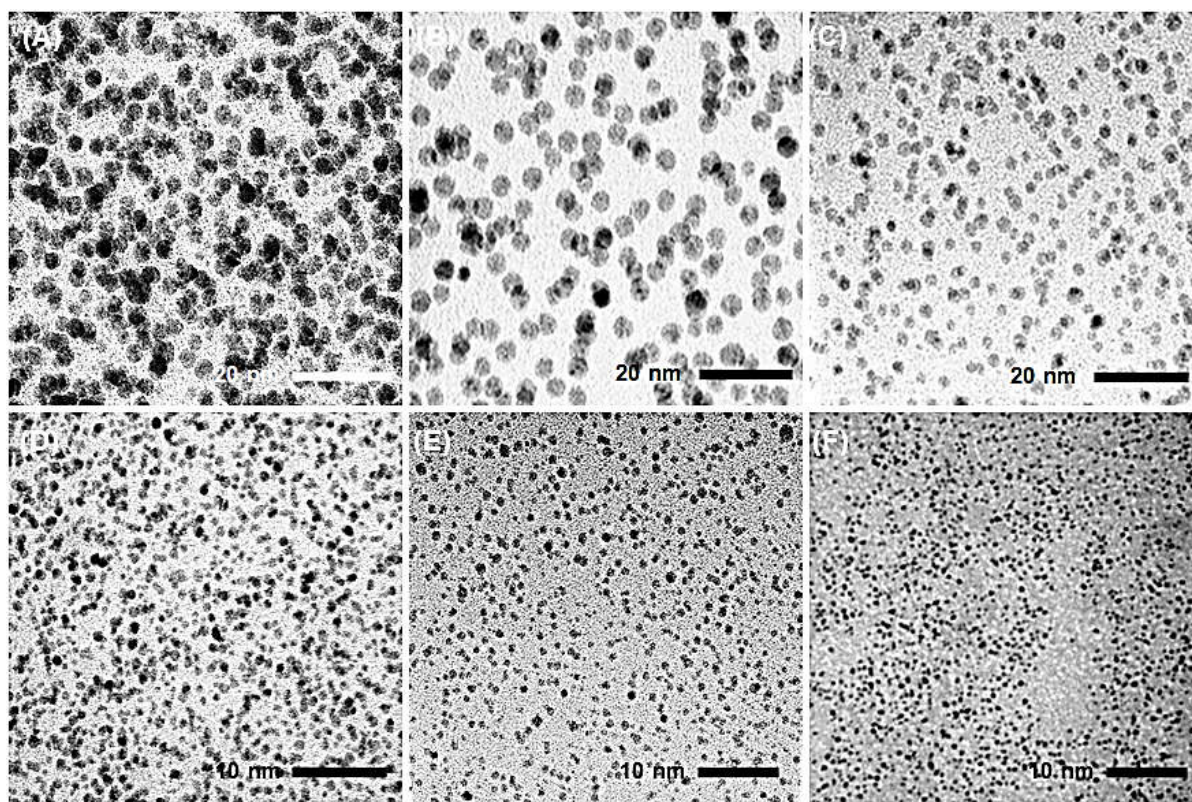


Figure 4. TEM images of AgNPs generated by the hydrazine-reduction of AgNO₃ in different BAIIIs-based microemulsions: (A) 3a, (B) 3b, (C) 3c, (D) 3d, (E) 3e, and (F) 3f.

2.4.2. Particle Size Distribution (PSD)

The size histograms of the AgNPs obtained by BAIIIs (Figure 5) show that the nanoparticles have a very narrow PSD and are either not agglomerated or exhibit very little agglomeration. Uniformly dispersed AgNPs with a mean diameter of 1.5 ± 0.5 nm were produced by using the BAIII 3f with the highest surface steric energy (69.772 kcal/mol) as a stabilizing agent. In contrast, when using BAIII 3a of lowest surface steric energy (50.029 kcal/mol) as a medium for AgNPs production, the AgNPs with a mean diameter of 2.9 ± 0.6 nm were obtained coupled with few agglomerated big AgNPs cluster of 4–5 nm.

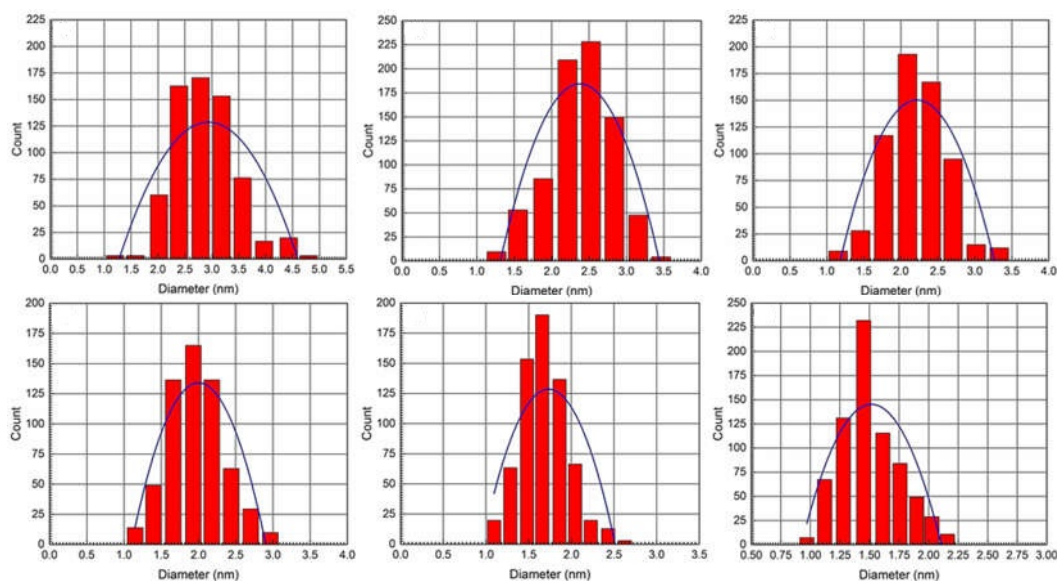


Figure 5. PSD histograms of AgNPs obtained using different BAILLs-based microemulsions.

2.5. Antibacterial Assay

The *in vitro* antibacterial activity of BAILLs-coated AgNPs was evaluated in comparison to that of Ciprofloxacin (Cipro) (a clinical antibiotic used for treating skin bacterial infections) using three of the most common ESKAPE infections found in contaminated food. Initially, the antibacterial efficacy of each sample was measured using the inhibition zone diameter (IZD, mm). As can be seen in Figure 6, all AgNPs have the capacity to limit the growth of all tested bacterial cells; however, their efficacy varies depending on the kind of bacterium, BAILL structural characteristics, and AgNPs' mean size. Noteworthy, the gram-positive (G^+) bacterial strain (*SA*) was generally more susceptible to all treatments than gram-negative (G^-) ones (*PA* and *KP*). The structural differences between the outer bacterial walls of the two types may be to blame for the different inclination of bacterial membrane permeability and, as a result, bactericidal effects. Particularly, unlike the G^+ —bacterial wall that contains only a thin peptidoglycan layer, G^- bacteria have a more sophisticated outer membrane that may operate as a barrier to the invasion of antibiotics into bacterial cells due to the presence of phospholipids (PLs), lipopolysaccharides (LPS), and lipoproteins (LPs) [36]. Interestingly, the IZD data indicate that the antibacterial activity of AgNPs improves as their mean size falls. For example, the AgNPs of the smallest size (1.5 nm), obtained using BAILL **3f**, exhibit the highest activity against *SA* (43.59 ± 1.48 mm). In contrast, the antistaphylococcal activity (24.31 ± 0.79 mm) is lowest for the biggest AgNPs (2.9 nm), which were made using BAILL **3a**. The findings of CFU method and CFU/mL values are in good consistency with the results obtained by AWD method. As shown in Figure 6A–C and S2 (SM⁺), a remarkable bacterial reduction was observed in all bacterial cells after treatment with BAILL-coated AgNPs; however, the performance depends on the bacterial strain type, the ionic liquid coating, and the AgNPs' sizes. Overall, the G^+ strain (*SA*) was more sensitive to AgNPs, and its bacterial colony count was reduced by a value of 72–92% after treatment. In contrast, G^- bacteria (*PA* and *KP*) were less responsive to AgNPs treatments and showed bacterial colony reductions (BCR) of 58–81% and 54–75%, respectively, in AgNPs-treated *PA* and *KP* samples in comparison to growth controls.

It is worth noting that the butylimidazolium-coated AgNPs (AgNPs-3d, AgNPs-3e, and AgNPs-3f) (BCR 68–92%) are more potent antibiotics than methylimidazolium-coated AgNPs (AgNPs-3a, AgNPs-3b, and AgNPs-3c) (BCR 54–77%). Antibiotic activity (BCR 71–92%) is greatest for AgNPs with a mean particle size of 1.5 nm.

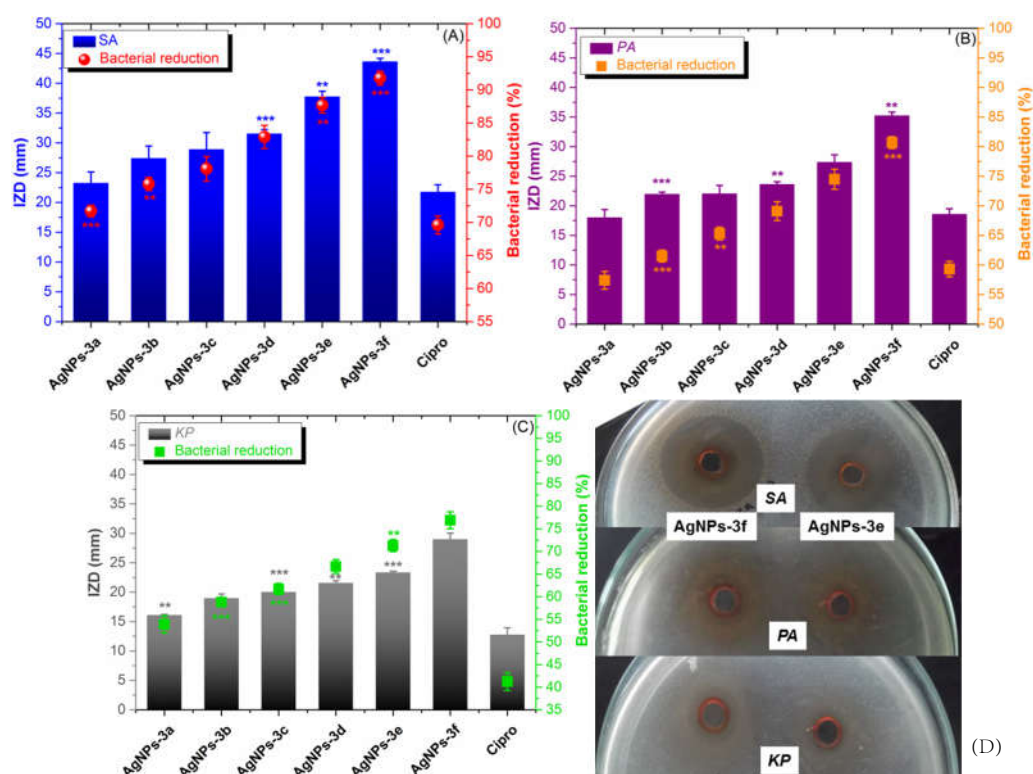


Figure 6. Graph for the inhibition zone diameter (IZD, mm) and the percentage of bacterial colonies reduction (%) for the examined AgNPs against (A) G^+ bacteria (SA), (B) G^- bacteria (PA), and (C) G^- bacteria (KP) (** $p < 0.005$, *** $p < 0.001$). (D) Photographs of inhibition zones for the most active antibiotics (AgNPs-3e and AgNPs-3f).

Once more, Table 2 MIC and MBC values demonstrate that G^+ -bacterium was more sensitive to AgNPs than G^- species. The presence of negatively charged phosphate groups on its surface may also play a role in this [37]. The positively charged nanoparticles can interact strongly with these groups. The extent to which AgNPs exhibited bactericidal or bacteriostatic actions was also significantly influenced by the type of tested bacteria and the NPs size. For example, the AgNPs coated by 4-tert-butylbenzyl-substituted BAILL (3f) were the most potent antibiotic for SA (MIC/MCB = $0.25 \pm 0.12/0.35 \pm 0.16 \mu\text{g/mL}$).

Table 2. MIC and MBC values ($\mu\text{g/mL}$) of new BAILLs-supported AgNPs against ESKAPE pathogens, as compared to clinical antibiotics (GM and TC).

Sample	Size (nm)	SA		PA		KB	
		MIC \pm SD	MBC \pm SD	MIC \pm SD	MBC \pm SD	MIC \pm SD	MBC \pm SD
AgNPs-3a	2.9	3.25 ± 0.25	3.75 ± 0.31	8.76 ± 0.32	8.85 ± 0.35	9.32 ± 0.34	9.50 ± 0.37
AgNPs-3b	2.4	2.25 ± 0.12	2.25 ± 0.15	7.07 ± 0.19	7.15 ± 0.45	8.87 ± 0.11	8.05 ± 0.25
AgNPs-3c	2.2	1.95 ± 0.15	2.07 ± 0.19	5.85 ± 0.25	5.95 ± 0.33	7.35 ± 0.37	7.48 ± 0.33
AgNPs-3d	2.0	1.76 ± 0.15	1.95 ± 0.11	5.55 ± 0.29	5.65 ± 0.37	7.15 ± 0.21	7.23 ± 0.25
AgNPs-3e	1.7	0.85 ± 0.11	0.95 ± 0.23	2.75 ± 0.36	2.85 ± 0.45	4.45 ± 0.29	4.55 ± 0.41
AgNPs-3f	1.5	0.25 ± 0.12	0.35 ± 0.18	1.36 ± 0.27	1.39 ± 0.28	2.22 ± 0.15	2.25 ± 0.19
Cipro	-	5.20 ± 0.16	5.75 ± 0.25	7.75 ± 0.23	8.05 ± 0.31	10.13 ± 0.56	10.55 ± 0.48

NA = not assigned.

On the other hand, AgNPs obtained by nascent benzyl-imidazolium BAILL (3a) were the least active anti-staphylococcal agent (MIC/MCB = $3.25 \pm 0.25/3.75 \pm 0.31 \mu\text{g/mL}$). It is worth noting that with MIC/MCB values between $2.22 \pm 0.15/2.25 \pm 0.19 \mu\text{g/mL}$ and $9.32 \pm 0.34/9.50 \pm 0.37 \mu\text{g/mL}$, KP is the most drug-resistant strain of bacteria.

2.6. Anti-Biofilm Activity

The ability of the most potent antibiotics (AgNPs-3d, AgNPs-3e, and AgNPs-3f) to prevent the development of bacterial biofilm on polystyrene surfaces was evaluated in vitro as compared to a positive control (Cipro) and a growth control (deionized water, DIW). As can be seen in Figure 7, all of the materials studied strongly limit the formation of bacterial biofilms, albeit this capacity varies depending on material structure and bacterial type. Specifically, the G⁺ bacterial biofilm (*staphylococcal* biofilm) formation is inhibited by AgNPs more so than by G[−] bacterial (*PA* and *KP*) biofilms. Furthermore, it is evident that AgNPs impeded *PA* biofilm formation more so than *KP* biofilm production ($p < 0.005$). Among the tested AgNPs, (tert-butyl)benzyl)-butylimidazolium-coated AgNPs (AgNPs-3f) was the most effective anti-biofilm agent, inhibiting bacterial biofilm formation by approximately 96%, 89%, and 78% for *SA*, *PA*, and *KP*, respectively, which was 1.5- to 2-fold higher than the effects induced by the positive control (Cipro). These findings suggest that the increased activity of AgNPs in preventing bacterial biofilm formation is due to its strong antimicrobial impact on the bacterial cells submerged in cultures or biofilms, and their ability to restrict adhesion of bacterial cells onto the NPs-coated polystyrene surfaces.

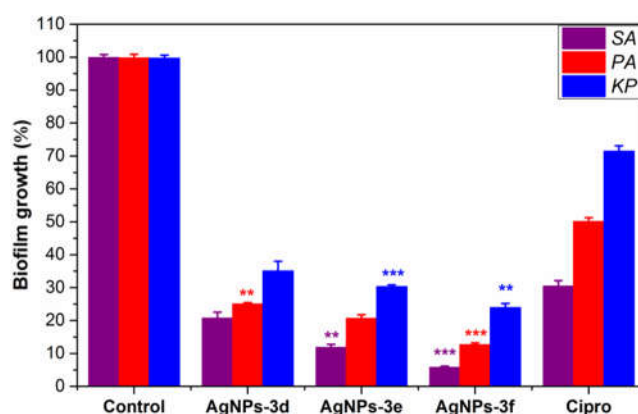


Figure 7. Inhibition of bacterial biofilm formation by the most potent antibiotics (AgNPs-3d, AgNPs-3e, and AgNPs-3f) as compared to a positive control (Cipro) and negative control (DI water), (** $p < 0.005$, *** $p < 0.001$).

2.7. In Vitro Cytotoxicity

New BAIILs-coated AgNPs were tested for cytotoxicity against normal (HSF) cells using the MTT assay in comparison to the positive control, cisplatin (CDDP). It is common practice to conduct initial single-dose studies of novel drugs for cytotoxic effects in human cell lines. Therefore, we looked at how BAIILs-coated AgNPs affected HSF cell proliferation when used in a single dose (10 $\mu\text{g}/\text{mL}$) (Figure 8A). The cytotoxicity data showed that all BAIILs-coated AgNPs are significantly ($p < 0.0001$) less toxic than CDDP toward HSF cells. In addition, the AgNPs derived from the butylimidazolium-supported BAIILs (3d–f) (AgNPs-3d, AgNPs-3e, and AgNPs-3f) are more toxic for HSF cells than the AgNPs obtained from the methylimidazolium-supported BAIILs (3a–c). Meanwhile, according to IC_{50} values (Figure 8B), the clinical drug (CDDP) is more toxic to healthy cells than all new TBAIILs-AgNPs. BAIIL coatings are proving to be an effective tool in reducing the toxic effects of silver nanoparticles on normal cells. This new innovative solution is based on using BAIILs covalently bound to the silver nanoparticles. These ILs act to reduce the release of silver ions, which are typically the most toxic components. According to our findings, this study provides hope for the future development of safe and promising BAIILs-AgNPs-based microemulsions as bacterial infection medications, particularly for skin bacterial infections.

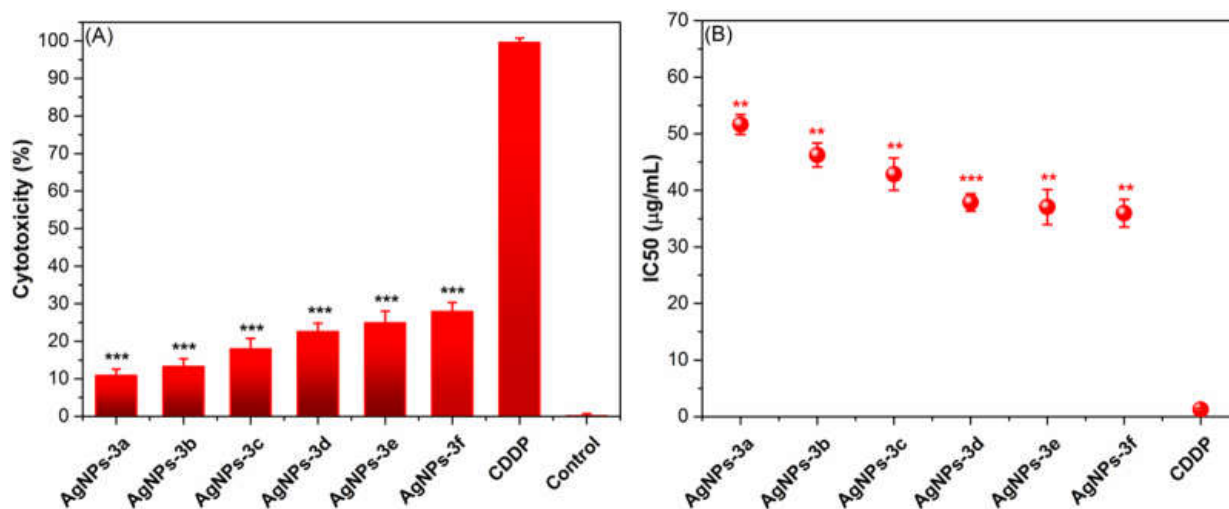


Figure 8. (A) A single dose (10 µg/mL) inhibitory impacts of BAIIILs-AgNPs on the proliferation of HSF cell lines. (B) Values of IC₅₀ (µg/mL) for BAIIILs-AgNPs against HSF in comparison to CDDP (** $p < 0.005$, *** $p < 0.001$).

2.8. Proposed Mechanism for Pharmacological Activity of New BAIIILs-AgNPs

There is still much uncertainty about how NMNPs exert their beneficial effects on bacteria or cancer. However, the high biocompatibility and excellent photothermal effects of AgNPs may greatly contribute to their superior bioactivity [38]. In addition, the ability of BAIIIL-coated AgNPs to adhere to the bacterial membrane by electrostatic binding between the negatively charged bacterial cell and the positively charged NPs and BAIIIL is critical for their bactericidal activity. This breaks the integrity of the bacterial membrane, leading to cell death [39]. Moreover, the extremely small sizes (2.9–1.5 nm) and unique hydrophobic coatings (BAIIILs) enable these NPs to enter bacterial cells without being ingested by endocytosis and to subsequently aggregate within the cells, where they can exert a wide range of antimicrobial effects [39,40]. According to Jiang et al., silver nanoparticles release silver ions that interact with the thiol groups of many enzymes, rendering most of the respiratory chain enzymes inactive and thereby triggering the formation of reactive oxygen species (ROS), which in turn triggers the bacterial cell's own self-destruction and that of the cancer cell as well [41]. Additionally, silver works as a soft acid that interacts readily with the nitrogen, sulphur, and phosphorus bases of DNA to inactivate its replication, so rendering the nuclear machinery of the cell inoperable [42]. Eventually, it could be speculated that the surface area to volume ratio of AgNPs has a significant impact in providing pharmacological activity. The presence of BAIIILs capping nanoparticles confers a unique surface functionality, causing them to interact with various cell types in a predetermined fashion (see Figure 9). The effectiveness of pharmacological activity increases as particle size decreases. Additionally, the BAIIIL coating plays an important role in the enhancing the antibacterial action of AgNPs in multiple possible ways: (i) the effects on bacterial cell walls due to interactions between cationic imidazolium group and their negative charge; (ii) the capabilities of hydrophobic alkyl substituents to aid AgNPs in penetrating lipophilic cell membranes [43]; and (iii) changes in membrane structure and dynamics as a result of exposure to imidazolium-based ionic liquids. Specifically, the imidazolium-based ionic liquids caused changes in the lipid bilayer of the cell membrane, leading to an increase in membrane permeability and cellular damage [44].

Comparing the antibacterial activity of newly developed BAIIILs-capped AgNPs with that of previously reported counterparts (see Table S1, Supplementary Materials), [45,46] revealed that the BAIIILs-AgNPs had significantly higher antibacterial efficacies (with MIC/MBC values in the range of 0.25/0.35–2.22/2.25 µg/mL) than the previously reported AgNPs (with MIC/MBC values in the range of 16/16–256/256 µg/mL). These results demonstrate that the new AgNPs have both higher MIC values as well as higher MBC

values in comparison to previously reported ionic liquid-coated AgNPs. This indicates that the new AgNPs are more effective in controlling bacteria growth than their previously studied counterparts. Thus, the new AgNPs could potentially be an effective and safe alternative to treat bacterial infections more effectively.

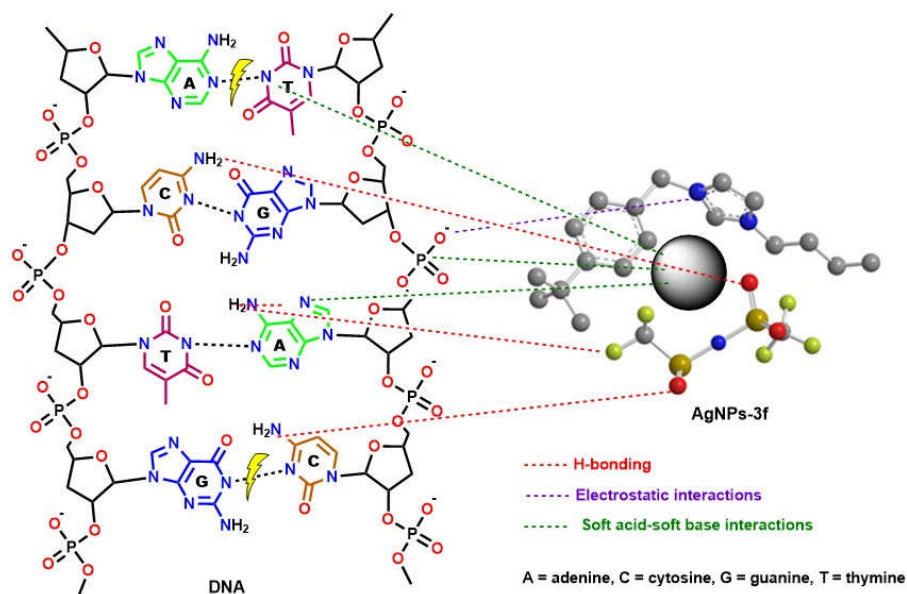


Figure 9. The proposed mechanism for DNA-cleavage activity of new thiazolium AgNPs-3f.

Notably, the alkyl chain length of BAILs plays vital roles both in the steric stabilization of AgNPs as well as their antibacterial capabilities. The findings of the previous studies indicate that increasing the chain length of the ionic liquid can enhance the steric stabilization of AgNPs, which can be attributed to the increased number of hydrophobic interactions between the ionic liquid molecules and the AgNPs [45,46]. In addition, increasing the alkyl chain length of an imidazolium ionic liquid can lead to an increase in its antimicrobial effectiveness. The findings are in agreement with a study conducted by Docherty and Kulpa [47] which revealed that chain length has a significant impact on the antimicrobial potency of the ionic liquids. The researchers found that increasing the chain length from C1 to C4 resulted in a significant increase in antibacterial activity against Gram-positive and Gram-negative bacteria. In particular, the C4 derivative was observed to be the most effective with a minimum inhibitory concentration (MIC) of 8.25 mM against G^+ -bacteria and 4.03 mM against G^- -bacteria. The increased antibacterial activity was due to an increased partition coefficient of the ionic liquid, which allowed it to be more effectively absorbed by the cellular membrane of the bacteria.

3. Materials and Methods

Chemical and solvent suppliers and their details were provided in the Supplementary Materials (Supplementary Materials). In addition, the preparation and characterization of benzyl chloride (R^1BnCl) derivatives (**1a–c**) and benzyl alkyl imidazolium chloride $[R^1BnImR^2]^+Cl^-$ ionic liquids (**2a–f**) were described in the Supplementary Materials.

The new BAILs were structurally characterized based upon the spectral analyses (FTIR, UV-Vis, NMR (1H NMR, ^{13}C NMR, ^{19}F NMR), and ESI-MS) and physical measurements. The detail for these instruments were also provided in the Supplementary Materials.

3.1. Synthesis of Tunable Benzyl Alkyl Imidazolium Ionic Liquids (BAILs, **3a–f**)

While vigorously stirring, a solution of lithium bis(trifluoromethanesulfonimide) ($LiTf_2N$) (6.66 g, 0.03 mol) in a combination of ACN (10 mL) and deionized water (DIW) (10 mL) was added dropwise to a solution of $[R^1BzR^2Im]Cl$ (**2a–f**) (0.03 mol) in DIW. The

resulting mixture was then magnetically stirred overnight at room temperature. After the reaction time was completed and the aqueous layer was discarded, the oily residues were dissolved in dichloromethane (DCM) and repeatedly washed with DIW until there was no precipitation of the AgNO₃ solution with the washing water. The resulting oily products were subsequently vacuum-dried for 48 hours at 343 K to remove any leftover water. Samples of the produced BAIIIIs (**3a–f**) were characterized as follow:

3-benzyl-1-methylimidazolium bis((trifluoromethyl)sulfonyl)amide [BnMIm][Tf₂N] (**3a**): Obtained in a 95% yield. ¹H NMR (500 MHz, CDCl₃) δ (ppm); 9.41 (1H, s, Im-H), 7.90 (1H, d, J = 1.8 Hz, Im-H), 7.72 (1H, d, J = 1.8 Hz, Im-H), 7.70–7.49 (5H, m, Ar-H), 5.38 (2H, 2, Ph-CH₂), 3.87 (3H, s, N-CH₃). ¹³C NMR (75 MHz, CDCl₃) δ (ppm): 149.87, 139.96, 137.38, 131.42, 129.56, 126.21, 124.51, 122.98, 56.39, and 37.63. ¹⁹F NMR (565 MHz, CDCl₃): singlet at δ –81.67 ppm (Tf₂N-CF₃). ESI-MS (positive mode): 173.2 *m/z* [M – Tf₂N[–], C₁₁H₁₃N₂]⁺.

3-(4-isopropylbenzyl)-1-methylimidazolium bis((trifluoromethyl)sulfonyl)amide [^{iso}PBnMIm][Tf₂N] (**3b**): Obtained in a 87% yield. ¹H NMR (500 MHz, CDCl₃) δ (ppm); 9.35 (1H, s, Im-H), 7.96 (1H, d, J = 1.9 Hz, Im-H), 7.74 (1H, d, J = 1.9 Hz, Im-H), 7.38–7.16 (4H, m, Ar-H), 5.39 (2H, 2, Ar-CH₂), 3.98 (3H, s, N-CH₃), 3.78 (1H, p, J = 1.9 Hz, CH(CH₃)₂), 1.24 (6H, d, J = 6.9 Hz, CH(CH₃)₂). ¹³C NMR (75 MHz, CDCl₃) δ (ppm): 148.92, 146.07, 137.61, 133.88, 130.64, 126.33, 123.06, 122.31, 56.31, 37.17, 33.31, and 23.21. ¹⁹F NMR (565 MHz, CDCl₃): singlet at δ –81.69 ppm (Tf₂N-CF₃). ESI-MS (positive mode): 215.2 *m/z* [M – Tf₂N[–], C₁₄H₁₉N₂]⁺.

3-(4-(^{tert}butyl)benzyl)-1-methylimidazolium bis((trifluoromethyl)sulfonyl)amide [^{tert}BBnMIm][Tf₂N] (**3c**): Obtained in a 91% yield. ¹H NMR (500 MHz, CDCl₃) δ (ppm); 9.88 (1H, s, Im-H), 7.93 (1H, d, J = 2.0 Hz, Im-H), 7.74 (1H, d, J = 2.0 Hz, Im-H), 7.49–7.23 (4H, m, Ar-H), 5.39 (2H, 2, Ar-CH₂), 3.89 (3H, s, N-CH₃), 1.38 (9H, s, C(CH₃)₃). ¹³C NMR (126 MHz, CDCl₃) δ (ppm): 149.76, 148.57, 138.64, 131.95, 129.13, 125.15, 123.88, 122.96, 55.63, 37.74, 34.34, and 31.91. ¹⁹F NMR (565 MHz, CDCl₃): singlet at δ –81.65 ppm (Tf₂N-CF₃). ESI-MS (positive mode): 229.2 *m/z* [M – Tf₂N[–], C₁₅H₂₁N₂]⁺.

3-benzyl-1-butylimidazolium bis((trifluoromethyl)sulfonyl)amide [BnBIm][Tf₂N] (**3d**): Obtained in a 91% yield. ¹H NMR (500 MHz, CDCl₃) δ (ppm); 9.26 (1H, s, Im-H), 7.84 (1H, d, J = 1.8 Hz, Im-H), 7.78 (1H, d, J = 1.7 Hz, Im-H), 7.61–7.36 (5H, m, Ar-H), 5.35 (2H, 2, Ph-CH₂), 4.19 (2H, t, J = 7.2 Hz, N-CH₂CH₂CH₂CH₃), 1.79 (2H, p, J = 7.2 Hz, N-CH₂CH₂CH₂CH₃), 1.27 (2H, m₍₆₎, N-CH₂CH₂CH₂CH₃), 0.91 (3H, t, J = 7.3 Hz, N-CH₂CH₂CH₂CH₃). ¹³C NMR (126 MHz, CDCl₃) δ (ppm): 149.68, 137.93, 134.63, 129.24, 128.74, 126.02, 123.14, 122.89, 55.24, 47.44, 31.60, 19.16, and 13.60. ¹⁹F NMR (565 MHz, CDCl₃): singlet at δ –81.66 ppm (Tf₂N-CF₃). ESI-MS (positive mode): 215.2 *m/z* [M – Tf₂N[–], C₁₄H₁₉N₂]⁺.

3-(4-isopropylbenzyl)-1-butylimidazolium bis((trifluoromethyl)sulfonyl)amide [^{iso}PBnBIm][Tf₂N] (**3e**): Obtained in a 85% yield. ¹H NMR (500 MHz, CDCl₃) δ (ppm); 9.91 (1H, s, Im-H), 7.92 (1H, d, J = 2.2 Hz, Im-H), 7.72 (1H, d, J = 2.1 Hz, Im-H), 7.44–7.19 (4H, m, Ar-H), 5.64 (2H, 2, Ar-CH₂), 4.26 (2H, t, J = 7.4 Hz, N-CH₂CH₂CH₂CH₃), 3.28 (1H, p, J = 6.9 Hz, CH(CH₃)₂), 1.85 (2H, p, J = 7.2 Hz, N-CH₂CH₂CH₂CH₃), 1.33 (2H, m₍₆₎, N-CH₂CH₂CH₂CH₃), 1.19 (6H, d, J = 7.1 Hz, CH(CH₃)₂) 0.91 (3H, t, J = 7.3 Hz, N-CH₂CH₂CH₂CH₃). ¹³C NMR (126 MHz, CDCl₃) δ (ppm): 149.65, 146.03, 138.91, 134.53, 129.38, 128.57, 125.64, 123.58, 122.54, 55.75, 47.45, 32.38, 31.82, 23.23, 21.81, and 13.85. ¹⁹F NMR (565 MHz, CDCl₃): singlet at δ –81.67 ppm (Tf₂N-CF₃). ESI-MS (positive mode): 257.3 *m/z* [M – Tf₂N[–], C₁₇H₂₅N₂]⁺.

3-(4-(^{tert}butyl)benzyl)-1-butylimidazolium bis((trifluoromethyl)sulfonyl)amide [^{tert}BBnBIm][Tf₂N] (**3f**): Obtained in a 89% yield. ¹H NMR (500 MHz, CDCl₃) δ (ppm); 9.84 (1H, s, Im-H), 7.91 (1H, d, J = 2.1 Hz, Im-H), 7.74 (1H, d, J = 2.1 Hz, Im-H), 7.49–7.27 (4H, m, Ar-H), 5.61 (2H, 2, Ar-CH₂), 4.28 (2H, t, J = 7.3 Hz, N-CH₂CH₂CH₂CH₃), 1.83 (2H, p, J = 7.1 Hz, N-CH₂CH₂CH₂CH₃), 1.40 (9H, s, C(CH₃)₃), 1.31 (2H, m₍₆₎, N-CH₂CH₂CH₂CH₃), 1.19 (6H, d, J = 6.9 Hz, CH(CH₃)₂) 0.90 (3H, t, J = 7.2 Hz, N-CH₂CH₂CH₂CH₃). ¹³C NMR (126 MHz, CDCl₃) δ (ppm): 149.72, 148.51, 137.92, 131.65, 129.42, 125.64, 123.63, 122.91,

55.68, 47.52, 34.41, 33.34, 31.43, 21.21, and 13.87. ^{19}F NMR (565 MHz, CDCl_3): singlet at δ –81.69 ppm ($\text{Tf}_2\text{N-CF}_3$). ESI-MS (positive mode): 271.3 m/z [$\text{M} - \text{Tf}_2\text{N}^-$, $\text{C}_{18}\text{H}_{27}\text{N}_2$] $^+$

3.2. Preparation of IILMEs-Mediated AgNPs

With a minor tweak, we used the optimum conditions adopted from previously reported investigations [48–50] to fabricate the AgNPs in situ in the microemulsions containing the BAIIIs (3a–f). In brief, the BAIIIs/TX-100/ H_2O microemulsions (IILMEs) were first prepared by mixing 0.1 g of BAIIl and 1.4 g of TX-100 in deionized water (8.5 g) for 20 min at room temperature to ensure proper blending and formation of homogeneous solutions. Afterward, a 0.1 mmol aqueous AgNO_3 solution was added to this microemulsion and the mixture was agitated for 10 min. A diluted hydrazine hydrate solution (1 mL) was added and the reaction mixture was then stirred at 60 °C for 1 h. The solution color changes from a light yellow to a brownish yellow, which is evidence of the creation of silver nanoparticles. To ensure full reduction, a small amount of hydrazine hydrate was added. Moreover, UV-Visible spectroscopy scanning verified the production of AgNO_3 . Silver nanoparticles were recovered after being stabilized in a microemulsion system composed of AgNO_3 /BAIIIs/TX-100/ H_2O by centrifuging.

3.3. Antimicrobial Study

Three representative ESKAPE pathogens *PA* (ATCC-27853), *KP* (ATCC-13883), and *SA* (ATCC-29737) were utilized to test the antimicrobial power of the new BAIIl-supported AgNPs. Ciprofloxacin (Cipro), the most common antibiotic used for skin bacterial treatments, was served as the “positive” control. The NODCAR in Cairo, Egypt, kindly supplied all of the bacterial species used in this study, and these bacteria were routinely cultured in nutrient broth agar (NBA). First, we inoculated Mueller–Hinton Broth (MHB) with a bacterial solution containing $\sim 10^6$ CFU/mL and incubated the mixture at 37 °C in a 5% CO_2 environment to establish the initial bacterial culture. We then used the Well diffusion assay (WDA) and colony forming unit (CFU) methods outlined in our previous work [51] to determine which bacterial strains were most sensitive to the novel AgNPs. The sizes of the inhibition zones (IZD, mm) were the most important factors in determining the NPs’ antibacterial effectiveness. For the CFU method, we used the following formula (Equation (1)) to determine the relative decline in bacterial colony numbers (R%):

$$\text{R\%} = \frac{\text{BC}_{CT} - \text{BC}_{TT}}{\text{BC}_{CT}} \quad (1)$$

where BC_{CT} and BC_{TT} are the number of bacterial colonies in growth control and treatment test tubes, respectively. The obtained results were determined using mean SEM from triplicates of each trial.

Minimal Inhibitory/Bactericidal Concentrations (MIC/MBC)

The antibacterial efficacy indicators, MIC and MBC, of new compounds against tested bacterial strains were determined using the microtitre broth dilution technique as described in our prior study [52]. In brief, the bacterial suspension was treated with AgNPs and antibiotics, separately, that had been pre-dispersed in DMSO and prediluted Mueller–Hinton Broth (MHB). After transferring 190 μL bacterial suspensions (10^6 CFU/mL) to 96-well microtiter plates, AgNPs with concentrations in the range of 0.25–50.0 g/mL were added, then the plates were left to incubate at 37 °C for 24 h; controls consisted of wells that had not been treated. The Well turbidity measurements were used to calculate MIC and MBC concentrations. In order to calculate the MIC and MBC, multiple independent replicates of each sample were evaluated. The results are shown as the mean \pm SEM.

3.4. Anti-Biofilm Study

According to our previously published work [52], the ability of the most effective antibiotics (**AgNPs-3d**, **AgNPs-3e**, and **AgNPs-3f**) to inhibit bacterial biofilm formation and

eradicate the biofilms created by the tested bacterial strains (SA, PA, and KP) was studied.

3.5. In Vitro Cytotoxicity Study

3.5.1. Cell Cultures

Healthy human skin fibroblast (HSF) cell lines were obtained from the American Type Cell Culture Collection (ATCC, Manassas, USA). Dulbecco's Modified Eagle's Medium (DMEM, Invitrogen/Life Technologies) was used to cultivate these cell lines, supplemented with 10% fetal bovine serum, 100 U/mL of penicillin, and 100 g/mL of streptomycin (HyClone, Thermo Scientific). The cells were maintained in a Thermo Scientific Heracell VIOS CO₂ incubator maintained at 37 °C with 5% CO₂ humidity.

3.5.2. In Vitro Anti-Proliferative Activity

The new BAILL-supported AgNPs were tested for their anti-breast cancer action in vitro using the MTT assay. Briefly, a 96-well plate (Falcon, NJ, USA) was used to treat cell lines (10⁵ cells/well) with a range of doses (1.56 – 50 µg/mL) of the tested substance, a positive control cisplatin (CDDP), and a negative control (DMSO). Sets of wells (consisting of three wells each) were assigned for each sample. Cells were incubated for 48 h at 37 °C in a 5% CO₂ atmosphere, after which they were fixed, washed, and stained with MTT reagent, and then re-incubated for an additional 4 h. The staining media was carefully removed from the plate after incubation, and 180 µL of acidified isopropanol/well was added. The plate was then agitated at ambient temperature with a MaxQ 2000 plate shaker (Thermo Fisher Scientific Inc., MI, USA) to dissolve the formazan crystals that had formed. In order to determine the vitality of the cells, the plate was next subjected to a spectrophotometric analysis using a Stat FaxR 4200 plate reader (Awareness Technology, Inc., FL, USA).

4. Conclusions

This work presents the synthesis and characterization of a new class of imidazolium-supported BAILLs. (3a–f) by employing spectral (FTIR, NMR, and ESI-MS), thermal, and viscosity techniques. BAILLs were used as media and stabilizing agents for hydrazine-hydrate-catalyzed AgNO₃ reduction in BAILLs/TX-100/H₂O microemulsions into extremely small AgNPs. Unlike more traditional approaches, this synthetic process permits the synthesis of AgNPs networks with narrower PSD. Interestingly, AgNPs isolated from the BAILL bearing the bulkiest substituents (*tert*-butyl and *n*-butyl) (3f) displayed almost no NPs agglomeration. This study demonstrates that a simple step can be taken to achieve well-separated AgNPs—the addition of an electron-donating bulky para-substituent on the phenyl ring of the benzyimidazolium cation. All of the AgNPs-BAILLs tested in the in vitro antibacterial assay against ESKAPE pathogens showed very strong antibiotic properties, as evidenced by their DIZ and MIC/MBC values. Additionally, Gram-negative bacterial strains were more treatment-resistant than Gram-positive ones. Human skin fibroblast (HSF) cell lines were employed in an MTT experiment to measure the growth inhibitory effects of new drugs. The MTT cytotoxicity assay showed that the novel AgNPs had no great effect on the HSF cells. Consequently, the BAILL-coated AgNPs could offer safe and promising antibiotic candidates for skin bacterial infection treatments.

Supplementary Materials: The following supporting information can be downloaded at: <https://www.mdpi.com/article/10.3390/antibiotics12020247/s1>, Figure S1: TG curves of TBAILLs. Figure S2: Photographs of inhibition zones for the most active antibiotics (AgNPs-3e and AgNPs-3f). Table S1: MIC and MBC values (µg/mL) of new BAILLs-supported AgNPs against different pathogens, in comparison to previously reported ones.

Author Contributions: F.A., funding acquisition, supervision, visualization, analyzing the data, and writing the original draft paper; O.A.A.A., funding acquisition, supervision, visualization, analyzing the data, and writing the original draft paper; I.K., methodology, analyzing the data, visualization, and writing the original draft paper; M.Y.A., funding acquisition, coordinating the biological studies work, and analyzed the data; E.F., visualization, analyzing the data, software, and writing the original draft paper; A.A.S. and S.E.I.E., biological studies, visualization, analyzing the data, and writing the original draft paper; R.F.M.E., coordinating the work, performed the synthesis and characterization, and writing the original draft paper, review & editing; W.A.E.-F., synthesis and the preliminary characterization, analyzing the data, visualization, analyzing the data, and writing the original draft paper. All authors have read and agreed to the published version of the manuscript.

Funding: This study was supported by Taif University Researchers Supporting Project number (TURSP-2020/222), Taif University, Taif, Saudi Arabia, and King Khalid University funding under grant number (R.G.P. 2/59/44).

Institutional Review Board Statement: Not applicable.

Informed Consent Statement: Not applicable.

Data Availability Statement: Not applicable.

Acknowledgments: The authors extend their appreciation to the Deanship of Scientific Research at Taif University for funding this work through Taif University Researchers Supporting Project number (TURSP-2020/222), Taif University, Taif, Saudi Arabia. In addition, the authors thank the Deanship of Scientific Research at King Khalid University for funding this work through large Groups (Project under grant number R.G.P. 2/59/44).

Conflicts of Interest: The authors declare no conflict of interest.

References

1. Ribeiro, A.I.; Dias, A.M.; Zille, A. Synergistic effects between metal nanoparticles and commercial antimicrobial agents: A Review. *ACS Appl. Nano Mater.* **2022**, *5*, 3030–3064. [[CrossRef](#)] [[PubMed](#)]
2. Ju, J.; Xie, Y.; Yu, H.; Guo, Y.; Cheng, Y.; Qian, H.; Yao, W. Synergistic interactions of plant essential oils with antimicrobial agents: A new antimicrobial therapy. *Crit. Rev. Food Sci. Nutr.* **2022**, *62*, 1740–1751. [[CrossRef](#)] [[PubMed](#)]
3. Larsson, D.; Flach, C.-F. Antibiotic resistance in the environment. *Nat. Rev. Microbiol.* **2022**, *20*, 257–269. [[CrossRef](#)] [[PubMed](#)]
4. Kailasa, S.K.; Joshi, D.J.; Kateshiya, M.R.; Koduru, J.R.; Malek, N.I. Review on the biomedical and sensing applications of nanomaterial-incorporated hydrogels. *Mater. Today Chem.* **2022**, *23*, 100746. [[CrossRef](#)]
5. Mohammadzadeh, V.; Barani, M.; Amiri, M.S.; Taghavizadeh Yazdi, M.E.; Hassanisaadi, M.; Rahdar, A.; Varma, R.S. Applications of plant-based nanoparticles in nanomedicine: A review. *Sustain. Chem. Pharm.* **2022**, *25*, 100606. [[CrossRef](#)]
6. Hassan, Y.A.; Khedr, A.I.M.; Alkabli, J.; Elshaarawy, R.F.M.; Nasr, A.M. Co-delivery of imidazolium Zn(II)salen and Origanum Syriacum essential oil by shrimp chitosan nanoparticles for antimicrobial applications. *Carbohydr. Polym.* **2021**, *260*, 117834. [[CrossRef](#)]
7. Azharuddin, M.; Zhu, G.H.; Das, D.; Ozgur, E.; Uzun, L.; Turner, A.P.F.; Patra, H.K. A repertoire of biomedical applications of noble metal nanoparticles. *Chem. Commun.* **2019**, *55*, 6964–6996. [[CrossRef](#)]
8. Iravani, S.; Varma, R.S. Advanced Drug Delivery Micro- and Nanosystems for Cardiovascular Diseases. *Molecules* **2022**, *27*, 5843. [[CrossRef](#)]
9. Chandrakala, V.; Aruna, V.; Angajala, G. Review on metal nanoparticles as nanocarriers: Current challenges and perspectives in drug delivery systems. *Emergent Mater.* **2022**, *5*, 1593–1615. [[CrossRef](#)]
10. Carvalho, S.G.; Araujo, V.H.S.; Dos Santos, A.M.; Duarte, J.L.; Silvestre, A.L.P.; Fonseca-Santos, B.; Villanova, J.C.O.; Gremião, M.P.D.; Chorilli, M. Advances and challenges in nanocarriers and nanomedicines for veterinary application. *Int. J. Pharm.* **2020**, *580*, 119214. [[CrossRef](#)]
11. Ye, L.; Cao, Z.; Liu, X.; Cui, Z.; Li, Z.; Liang, Y.; Zhu, S.; Wu, S. Noble metal-based nanomaterials as antibacterial agents. *J. Alloys Compd.* **2022**, *904*, 164091. [[CrossRef](#)]
12. Huq, M.A.; Ashrafudoulla, M.; Rahman, M.M.; Balusamy, S.R.; Akter, S. Green Synthesis and Potential Antibacterial Applications of Bioactive Silver Nanoparticles: A Review. *Polymers* **2022**, *14*, 742. [[CrossRef](#)] [[PubMed](#)]
13. Naganthran, A.; Verasoundarapandian, G.; Khalid, F.E.; Masarudin, M.J.; Zulkharnain, A.; Nawawi, N.M.; Karim, M.; Che Abdullah, C.A.; Ahmad, S.A. Synthesis, Characterization and Biomedical Application of Silver Nanoparticles. *Materials* **2022**, *15*, 427. [[CrossRef](#)] [[PubMed](#)]
14. Dorjnamjin, D.; Ariunaa, M.; Shim, Y.K. Synthesis of Silver Nanoparticles Using Hydroxyl Functionalized Ionic Liquids and Their Antimicrobial Activity. *Int. J. Mol. Sci.* **2008**, *9*, 807–820. [[CrossRef](#)] [[PubMed](#)]

15. Patil, R.S.; Kokate, M.R.; Salvi, P.P.; Kolekar, S.S. A novel one step synthesis of silver nanoparticles using room temperature ionic liquid and their biocidal activity. *Comptes Rendus Chim.* **2011**, *14*, 1122–1127. [[CrossRef](#)]
16. Aliakbari, E.; Nural, Y.; Zamiri, R.E.; Yabalak, E.; Mahdavi, M.; Yousefi, V. Design and synthesis of silver nanoparticle anchored poly(ionic liquid)s mesoporous for controlled anticancer drug delivery with antimicrobial effect. *Int. J. Environ. Health Res.* **2022**, *32*, 1–13. [[CrossRef](#)]
17. Ostwald, W. Blocking of Ostwald ripening allowing long-term stabilization. *Phys. Chem.* **1901**, *37*, 385.
18. Długosz, O.; Szostak, K.; Staroń, A.; Pulit-Prociak, J.; Banach, M. Methods for Reducing the Toxicity of Metal and Metal Oxide NPs as Biomedicine. *Materials* **2020**, *13*, 279. [[CrossRef](#)]
19. Ahrens, S.; Peritz, A.; Strassner, T. Tunable aryl alkyl ionic liquids (TAAILs): The next generation of ionic liquids. *Angew. Chem. Int. Ed.* **2009**, *48*, 7908–7910. [[CrossRef](#)]
20. Verma, C.; Ebenso, E.E.; Quraisi, M. Transition metal nanoparticles in ionic liquids: Synthesis and stabilization. *J. Mol. Liq.* **2019**, *276*, 826–849. [[CrossRef](#)]
21. Hassanpour, M.; Shahavi, M.H.; Heidari, G.; Kumar, A.; Nodehi, M.; Moghaddam, F.D.; Mohammadi, M.; Nikfarjam, N.; Sharifi, E.; Makvandi, P.; et al. Ionic liquid-mediated synthesis of metal nanostructures: Potential application in cancer diagnosis and therapy. *J. Ion. Liq.* **2022**, *2*, 100033. [[CrossRef](#)]
22. de Oliveira, P.F.M.; Torresi, R.M.; Emmerling, F.; Camargo, P.H.C. Challenges and opportunities in the bottom-up mechanochemical synthesis of noble metal nanoparticles. *J. Mater. Chem. A* **2020**, *8*, 16114–16141. [[CrossRef](#)]
23. Mangaiyarkarasi, R.; Priyanga, M.; Santhiya, N.; Umadevi, S. In situ preparation of palladium nanoparticles in ionic liquid crystal microemulsion and their application in Heck reaction. *J. Mol. Liq.* **2020**, *310*, 113241. [[CrossRef](#)]
24. Capek, I. Preparation of metal nanoparticles in water-in-oil (w/o) microemulsions. *Adv. Colloid Interface Sci.* **2004**, *110*, 49–74. [[CrossRef](#)]
25. Elshaarawy, R.F.M.; Eldeen, I.M.; Hassan, E.M. Efficient synthesis and evaluation of bis-pyridinium/bis-quinolinium metallosalophens as antibiotic and antitumor candidates. *J. Mol. Struct.* **2017**, *1128*, 162–173. [[CrossRef](#)]
26. Elshaarawy, R.F.M.; El-Azim, H.A.; Hegazy, W.H.; Mustafa, F.H.A.; Talkhan, T.A. Poly(ammonium/pyridinium)-chitosan Schiff base as a smart biosorbent for scavenging of Cu²⁺ ions from aqueous effluents. *Polym. Test.* **2020**, *83*, 106244. [[CrossRef](#)]
27. Refaee, A.A.; El-Naggar, M.E.; Mostafa, T.B.; Elshaarawy, R.F.M.; Nasr, A.M. Nano-bio finishing of cotton fabric with quaternized chitosan Schiff base-TiO₂-ZnO nanocomposites for antimicrobial and UV protection applications. *Eur. Polym. J.* **2022**, *166*, 111040. [[CrossRef](#)]
28. Alfaifi, M.Y.; Shati, A.A.; Elbehairi, S.E.I.; Elshaarawy, R.F.M.; Gad, E.M. Fine-tuning of the pharmacological potential of novel thiazolium ionic liquids by anion alteration. *RSC Adv.* **2022**, *12*, 458–469. [[CrossRef](#)]
29. Kraynov, A.; Müller, T.E. Concepts for the stabilization of metal nanoparticles in ionic liquids. *Appl. Ionic Liquids Sci. Technol.* **2011**, *9*, 235–260.
30. Sidek, N.; Manan, N.S.A.; Mohamad, S. Efficient removal of phenolic compounds from model oil using benzyl Imidazolium-based ionic liquids. *J. Mol. Liq.* **2017**, *240*, 794–802. [[CrossRef](#)]
31. El-Sayed, W.N.; Alkabli, J.; Althumayri, K.; Elshaarawy, R.F.M.; Ismail, L.A. Azomethine-functionalized task-specific ionic liquid for diversion of toxic metal ions in the aqueous environment into pharmacological nominates. *J. Mol. Liq.* **2021**, *322*, 114525. [[CrossRef](#)]
32. Ibrahim, H.K.; El-Tamany, S.H.; El-Shaarawy, R.F.; El-Deen, I.M. Synthesis and investigation of mass spectra of some novel benzimidazole derivatives. *Maced. J. Chem. Chem. Eng.* **2008**, *27*, 65–79. [[CrossRef](#)]
33. Vitucci, F.M.; Trequattrini, F.; Palumbo, O.; Brubach, J.B.; Roy, P.; Paolone, A. Infrared spectra of bis(trifluoromethanesulfonyl)imide based ionic liquids: Experiments and DFT simulations. *Vib. Spectrosc.* **2014**, *74*, 81–87. [[CrossRef](#)]
34. Amendola, V.; Bakr, O.M.; Stellacci, F. A Study of the Surface Plasmon Resonance of Silver Nanoparticles by the Discrete Dipole Approximation Method: Effect of Shape, Size, Structure, and Assembly. *Plasmonics* **2010**, *5*, 85–97. [[CrossRef](#)]
35. Galbraith, H.; Miller, T.B. Physicochemical effects of long chain fatty acids on bacterial cells and their protoplasts. *J. Appl. Bacteriol.* **1973**, *36*, 647–658. [[CrossRef](#)]
36. Clements, A.; Gaboriaud, F.; Duval, J.F.; Farn, J.L.; Jenney, A.W.; Lithgow, T.; Wijburg, O.L.; Hartland, E.L.; Strugnell, R.A. The major surface-associated saccharides of *Klebsiella pneumoniae* contribute to host cell association. *PLoS ONE* **2008**, *3*, e3817. [[CrossRef](#)]
37. Szewczyk, O.K.; Roszczenko, P.; Czarnomysy, R.; Bielawska, A.; Bielawski, K. An overview of the importance of transition-metal nanoparticles in cancer research. *Int. J. Mol. Sci.* **2022**, *23*, 6688. [[CrossRef](#)]
38. Gopinath, K.; Karthika, V.; Gowri, S.; Senthilkumar, V.; Kumaresan, S.; Arumugam, A. Antibacterial activity of ruthenium nanoparticles synthesized using *Gloriosa superba* L. leaf extract. *J. Nanostructure Chem.* **2014**, *4*, 83. [[CrossRef](#)]
39. Lewinski, N.; Colvin, V.; Drezek, R. Cytotoxicity of Nanoparticles. *Small* **2008**, *4*, 26–49. [[CrossRef](#)]
40. Jiang, H.S.; Zhang, Y.; Lu, Z.W.; Lebrun, R.; Gontero, B.; Li, W. Interaction between Silver Nanoparticles and Two Dehydrogenases: Role of Thiol Groups. *Small* **2019**, *15*, 1900860. [[CrossRef](#)]
41. Prabhu, S.; Poulouse, E.K. Silver nanoparticles: Mechanism of antimicrobial action, synthesis, medical applications, and toxicity effects. *Int. Nano Lett.* **2012**, *2*, 32. [[CrossRef](#)]
42. Riduan, S.N.; Zhang, Y. Imidazolium salts and their polymeric materials for biological applications. *Chem. Soc. Rev.* **2013**, *42*, 9055–9070. [[CrossRef](#)] [[PubMed](#)]

43. Bakshi, K.; Mitra, S.; Sharma, V.K.; Jayadev, M.S.K.; Sakai, V.G.; Mukhopadhyay, R.; Gupta, A.; Ghosh, S.K. Imidazolium-based ionic liquids cause mammalian cell death due to modulated structures and dynamics of cellular membrane. *Biochim. Et. Biophys. Acta (BBA)-Biomembr.* **2020**, *1862*, 183103. [[CrossRef](#)] [[PubMed](#)]
44. Gholami, A.; Shams, M.S.; Abbaszadegan, A.; Nabavizadeh, M. Ionic liquids as capping agents of silver nanoparticles. Part II: Antimicrobial and cytotoxic study. *Green Process. Synth.* **2021**, *10*, 585–593. [[CrossRef](#)]
45. Avirdi, E.; Paumo, H.K.; Kamdem, B.P.; Singh, M.B.; Kumari, K.; Katata-Seru, L.M.; Bahadur, I. Influence of cation (imidazolium based ionic liquids) as “smart” stabilizers for silver nanoparticles and their evaluation as antibacterial activity on *Escherichia coli*, *Staphylococcus aureus* and *Enterobacter cloacae*. *J. Mol. Liq.* **2023**, *369*, 120935. [[CrossRef](#)]
46. Docherty, K.M.; Kulpa, J.C.F. Toxicity and antimicrobial activity of imidazolium and pyridinium ionic liquids. *Green Chem.* **2005**, *7*, 185–189. [[CrossRef](#)]
47. Corrêa, C.M.; Bizeto, M.A.; Camilo, F.F. Direct synthesis of silver nanoparticles in ionic liquid. *J. Nanopart. Res.* **2016**, *18*, 132. [[CrossRef](#)]
48. Setua, P.; Pramanik, R.; Sarkar, S.; Ghatak, C.; Rao, V.G.; Sarkar, N.; Das, S.K. Synthesis of silver nanoparticle in imidazolium and pyridinium based ionic liquid reverse micelles: A step forward in nanostructure inorganic material in room temperature ionic liquid field. *J. Mol. Liq.* **2011**, *162*, 33–37. [[CrossRef](#)]
49. Sun, X.; Qiang, Q.; Yin, Z.; Wang, Z.; Ma, Y.; Zhao, C. Monodispersed silver-palladium nanoparticles for ethanol oxidation reaction achieved by controllable electrochemical synthesis from ionic liquid microemulsions. *J. Colloid Interface Sci.* **2019**, *557*, 450–457. [[CrossRef](#)]
50. Elshaarawy, R.F.; Tadros, H.R.; Abd El-Aal, R.M.; Mustafa, F.H.; Soliman, Y.A.; Hamed, M.A. Hybrid molecules comprising 1,2,4-triazole or diaminothiadiazole Schiff-bases and ionic liquid moieties as potent antibacterial and marine antibiofouling nominees. *J. Environ. Chem. Eng.* **2016**, *4*, 2754–2764. [[CrossRef](#)]
51. Elshaarawy, R.F.; Lan, Y.; Janiak, C. Oligonuclear homo- and mixed-valence manganese complexes based on thiophene- or aryl-carboxylate ligation: Synthesis, characterization and magnetic studies. *Inorg. Chim. Acta* **2013**, *401*, 85–94. [[CrossRef](#)]
52. Elshaarawy, R.F.M.; Ismail, L.A.; Alfaifi, M.Y.; Rizk, M.A.; Eltamany, E.E.; Janiak, C. Inhibitory activity of biofunctionalized silver-capped N-methylated water-soluble chitosan thiomers for microbial and biofilm infections. *Int. J. Biol. Macromol.* **2020**, *152*, 709–717. [[CrossRef](#)] [[PubMed](#)]

Disclaimer/Publisher’s Note: The statements, opinions and data contained in all publications are solely those of the individual author(s) and contributor(s) and not of MDPI and/or the editor(s). MDPI and/or the editor(s) disclaim responsibility for any injury to people or property resulting from any ideas, methods, instructions or products referred to in the content.